

Frequency-Separable Hamiltonian Neural Network for Multi-Timescale Dynamics

Yaojun Li Yulong Yang Christine Allen-Blanchette[†]
 Princeton University, USA
 {y13425, yulong.yang, ca15}@princeton.edu

Abstract

While Hamiltonian mechanics provides a powerful inductive bias for neural networks modeling dynamical systems, Hamiltonian Neural Networks and their variants often fail to capture complex temporal dynamics spanning multiple timescales. This limitation is commonly linked to the spectral bias of deep neural networks, which favors learning low-frequency, slow-varying dynamics. Prior approaches have sought to address this issue through symplectic integration schemes that enforce energy conservation or by incorporating geometric constraints to impose structure on the configuration-space. However, such methods either remain limited in their ability to fully capture multiscale dynamics or require substantial domain specific assumptions. In this work, we exploit the observation that Hamiltonian functions admit decompositions into explicit fast and slow modes and can be reconstructed from these components. We introduce the Frequency-Separable Hamiltonian Neural Network (FS-HNN), which parameterizes the system Hamiltonian using multiple networks, each governed by Hamiltonian dynamics and trained on data sampled at distinct timescales. We further extend this framework to partial differential equations by learning a state- and boundary-conditioned symplectic operators. Empirically, we show that FS-HNN improves long-horizon extrapolation performance on challenging dynamical systems and generalizes across a broad range of ODE and PDE problems.

1 Introduction

Deep learning architectures have increasingly succeeded in replacing traditional numerical solvers for simulating and predicting the dynamics of complex systems (Brunton et al., 2016; Chen et al., 2018; Raissi et al., 2019; Li et al., 2020; Lu et al., 2021). Early efforts focused on modeling dynamics with black-box and recurrent models (Jordan, 1997; Hochreiter & Schmidhuber, 1997), whose expressivity is largely driven by increased parameter counts, often at the expense of interpretability. This trade-off can yield models that generalize poorly to dynamics that are not well represented in the training regime. Contemporary architectures attempt to address these limitations by incorporating inductive biases derived from physical laws (Greydanus et al., 2019; Toth et al., 2019; Lutter et al., 2019; Chen et al., 2019; Zhong et al., 2019; Cranmer et al., 2020; Allen-Blanchette et al., 2020), such as conservation of energy, rather than relying on purely black-box processes.

Hamiltonian mechanics has emerged as a popular approach for enforcing physical consistency in neural networks due to its broad applicability to systems that exhibit energy conservation. Early implementations (Greydanus et al., 2019; Toth et al., 2019) parameterized the system Hamiltonian with neural networks and computed dynamical updates using Hamilton’s equations. While these architectures showed significantly improved generalization and training efficiency compared to baseline MLPs, they enforced energy conservation only via soft constraints. As a result, the learned system often exhibits drift in total energy as the roll-out horizon increases (Chen et al., 2019). Subsequent

Preprint. [†] Corresponding author.

architectures have addressed this issue by incorporating the geometric structure of the underlying configuration space (Finzi et al., 2020b; Zhong & Leonard, 2020; Mason et al., 2022, 2023), encouraging dynamics to evolve on the correct manifold. However, this typically requires substantial *a priori* knowledge of the system, which may be unavailable for more general dynamical systems. A more principled approach enforces symplecticity in the dynamics updates (Zhong et al., 2019; Chen et al., 2019; Jin et al., 2020; Allen-Blanchette, 2024; Liu et al., 2025). Rather than learning the Hamiltonian directly, this line of work learns a symplectic map and reconstructs the Hamiltonian via the Hamilton–Jacobi equation (Cattaneo et al., 2011). By not tying the formulation directly to Hamilton’s principle, these methods are applicable to a broader class of dynamical systems. In practice, however, they still do not resolve the difficulty deep learning architectures face in capturing stiff dynamics, in part due to the spectral bias of neural networks favoring slow-varying low-frequency modes first (Rahaman et al., 2019; Xu et al., 2019).

While symplectic and Hamiltonian inductive biases are well studied for a broad range of ODE systems, it has garnered much less attention when modeling PDE systems. This contrast can be attributed, in large part, to the fact that PDE systems exhibit a variable symplectic operator that depends on system states, boundary conditions, and discretizations (Bridges, 1997; Bridges & Reich, 2001), while those for canonical ODEs are state- and time-invariant (Channell & Scovel, 1990). A common heuristic is to apply symplectic architectures to semi-discretized PDEs (Jin et al., 2020). While this approach dramatically reduces error on long rollout prediction, it is highly dependent on the discretization. Others approach this problem by leveraging multiple networks to model the symplectic and non-symplectic components (Eidnes & Lye, 2024). However, this yields representations that are not necessarily unique and provide weaker theoretical guarantees.

In this paper, we propose Frequency-Separable Hamiltonian Neural Network (FS-HNN) for modeling dynamical systems with stiff, multi-timescale behavior. FS-HNN leverages the fact that such systems often admit a separation between slow and fast modes (Ober-Blöbaum et al., 2024). Rather than learning a single Hamiltonian with one monolithic network, FS-HNN parameterizes the system Hamiltonian as the sum of multiple components, each trained on trajectories sampled at a distinct temporal resolution. This frequency separated formulation improves long-horizon prediction by mitigating spectral bias and enabling accurate modeling of both slow and fast dynamics. Furthermore, FS-HNN extends to discretized PDE systems by learning the action of a state- and condition-dependent skew-symmetric operator, yielding a structure-preserving framework applicable to two-dimensional flow dynamics. We evaluate on a wide range of ODE systems including the Fermi-Pasta–Ulam–Tsingou (Fermi et al., 1955) system, as well as PDE benchmarks such as the incompressible Taylor-Green vortex (Taylor & Green, 1937). Across these tasks, FS-HNN achieves better long-horizon rollout accuracy compared to competitive baselines while better capturing physically meaningful behavior.

2 Related Work

Conservation constraints in deep learning. Predicting the motion of dynamical systems can offer insights into a variety of engineering applications such as dynamics and control (Khalil & Grizzle, 2002) and computational fluid dynamics (Blazek, 2015). System identification (Verhaegen & Verdult, 2007) approaches yield accurate representations with strong guarantees, but only when the analytical expression (Magal & Webb, 2018; Galioto & Gorodetsky, 2020a,b) or the general functional form (Brunton et al., 2016; Epperlein et al., 2015; Paredes et al., 2024; Richards et al., 2024) of the system is well defined and known a priori. Deep learning architectures circumvent this concern by making no assumptions on the system form (Chen et al., 2018; Raissi et al., 2019; Li et al., 2020; Lu et al., 2021), and trading interpretability for expressivity.

More recently, networks have turned to encoded physical conservation constraints to achieve both expressivity and interpretability. One popular approach is to leverage Hamiltonian mechanics to encourage conservation of energy. Early Hamiltonian-based neural networks (Greydanus et al., 2019; Bertalan et al., 2019; Toth et al., 2019) parameterized the Hamiltonian with black box networks, and evolve system states according to Hamilton’s equation through a soft penalty term. However, over long time horizons, the energy drift that results from non-symplectic integrators causes accumulation of phase space error and deterioration of predictive performance (Chen et al., 2019).

Much of the existing literature addresses this concern with additional geometric constraints. Efforts that incorporate geometric constraints either enforce configuration space structure Finzi et al. (2020a,b); Zhong & Leonard (2020); Mason et al. (2023); Duong et al. (2024); Horn et al. (2025), or symplecticity in forecasting. The former is limited to settings where configuration space structure is known a priori. The latter is more general and is typically achieved either by rolling out trajectories using symplectic integrators Chen et al. (2019); Zhong et al. (2019); Han et al. (2021), or learning a symplectic map instead of the system Hamiltonian Jin et al. (2020); Burby et al. (2020); Chen & Tao (2021). Notably, learning the symplectic map offers a framework to both reconstruct the Hamiltonian via the Hamilton–Jacobi equation Jin et al. (2020) as well as generalize to systems that are not Hamiltonian (Eidnes & Lye, 2024). While these works effectively enforce conservation constraints, they are not designed to capture temporally complex dynamics.

Modeling systems with multiple scales. Discretising the input space and using multiple scales to capture varying dynamics and features have been shown to significantly improve performance and stability in a wide range of computational applications such as numerical analysis (Mandel et al., 1988; Mandel & Parter, 1990) and computer vision (Müller et al., 2022; Wang et al., 2025). This approach is especially beneficial when studying stiff dynamical systems (Lee & Engquist, 2013), where fast and slow modes evolve on significantly different timescales. Deep learning networks have leveraged this observation to design networks that operate on multiple by decomposing timeseries using auto-correlation (Wu et al., 2021); learning on seasonal decompositions (Wang et al., 2024); enabling cascading resolution blocks using convolutional autoencoders (Farooq et al., 2024); adaptively learning on separate timescales using Mixture-of-Experts (Hu et al., 2025); and leveraging evolutionary Monte Carlo sampling to separate timescales (Yao et al., 2025). While these architectures all show improved generalization and performance on timeseries data that present with multiple timescales, they rely on black box models and/or statistical metrics when designing separate networks. Conversely, Ober-Blöbaum et al. (2024) leverages the fact that Lagrangian systems can be decomposed into slow and fast modes, where every mode still exhibits Lagrangian dynamics, to design a physically consistent algorithm for simulating stiff dynamical systems. In this paper, we propose FS-HNN, which leverages a similar separability of the Hamiltonian formalism to design a neural network that accommodates complex and stiff systems by modeling different temporal scales separately, but still conserves overall system energy.

3 Background

In this section, we briefly review Hamiltonian mechanics, how Hamiltonian Neural Networks (HNN) leverage this structure to learn energy-conserving vector fields, and the role of symplectic integrators in long-horizon prediction.

3.1 Hamiltonian Mechanics

Hamiltonian mechanics offers a reformulation of classical Newtonian mechanics, focusing on energy rather than forces to define the dynamics of a system (Goldstein et al., 2002; Marion, 2013). Hamilton’s principle states that the motion of a system over an interval follows a path such that the time integral of the Lagrangian is stationary, typically at a minimum value. This constraint allows for a principled approach to understanding the dynamics of complex systems. Concretely, a system’s Hamiltonian H is a scalar quantity defined with respect to the generalized coordinates $q(t)$ and generalized momentum $p(t)$. The dynamics of such a system are therefore defined using Hamilton’s equations as

$$\dot{q} = \frac{\partial H(q, p)}{\partial p}, \quad \dot{p} = -\frac{\partial H(q, p)}{\partial q}. \quad (1)$$

A Hamiltonian system therefore evolves on a phase space with coordinates (q, p) and dimension twice that of the degrees of freedom of the system. Denoting the concatenation of generalized position and momentum as $z = (q, p)$, the time derivative of the Hamiltonian is

$$\frac{dH}{dt} = \nabla_z H(z)^\top \dot{z} = \nabla_z H(z)^\top J \nabla_z H(z) = 0, \quad (2)$$

showing that energy is conserved along a trajectory. Additional details are provided in Appendix A.

3.2 Hamiltonian Neural Networks

Hamiltonian Neural Networks (HNNs) (Greydanus et al., 2019; Toth et al., 2019) parameterize the Hamiltonian of conservative systems using a black box MLP H_θ . Contrary to conventional recurrent networks (Jordan, 1997), the loss of HNNs encourages the alignment of the gradients

$$\mathcal{L}_{\text{HNN}} = \left\| \frac{\partial H_\theta}{\partial \mathbf{p}} - \frac{d\mathbf{q}}{dt} \right\|_2^2 + \left\| \frac{\partial H_\theta}{\partial \mathbf{q}} + \frac{d\mathbf{p}}{dt} \right\|_2^2, \quad (3)$$

in order to encourage conservation of energy in the learned representations and improve long-range stability compared to unstructured architectures. Updated states are obtained using automatic differentiation (Baydin et al., 2018) according to Equation (1), such that

$$z_{t+1} = z_t + \int_t^{t+1} \frac{dz}{d\tau} d\tau. \quad (4)$$

The state updates for an ODE system parameterized by generalized states z can be written in symplectic form as

$$\frac{dz}{dt} = \underbrace{\begin{bmatrix} 0 & \mathbf{I} \\ -\mathbf{I} & 0 \end{bmatrix}}_J \begin{bmatrix} \partial H / \partial q \\ \partial H / \partial p \end{bmatrix} = J \nabla_z H, \quad (5)$$

where J is the symplectic operator.

Furthermore, to address energy drift from numerical instability in HNNs, symplectic neural networks (Zhong et al., 2019; Chen et al., 2019) leverage the symplectic form and symplectic integration to reduce long-term energy drift and preserve geometric structure. By assuming that the Hamiltonian is separable,

$$H(q, p) = T(p) + V(q), \quad (6)$$

Hamilton’s equations become

$$\dot{q} = \frac{\partial H}{\partial p} = \frac{\partial T(p)}{\partial p}, \quad \dot{p} = -\frac{\partial H}{\partial q} = -\frac{\partial V(q)}{\partial q}. \quad (7)$$

One popular symplectic integrator is the (kick–drift–kick) leapfrog method, given by

$$p_{n+1/2} = p_n - 1/2\Delta t \frac{\partial V}{\partial q}(q_n), \quad (8)$$

$$q_{n+1} = q_n + \Delta t \frac{\partial T}{\partial p}(p_{n+1/2}), \quad (9)$$

$$p_{n+1} = p_{n+1/2} - 1/2\Delta t \frac{\partial V}{\partial q}(q_{n+1}). \quad (10)$$

4 Methodology

In this section, we introduce the Frequency-Separable Hamiltonian Neural Network (FS-HNN). FS-HNN extends structure-preserving Hamiltonian learning from ODE systems with fixed symplectic structure Chen et al. (2019); Zhong et al. (2019); Jin et al. (2020) to discretized PDE systems by learning the action of a state- and condition-dependent skew-symmetric operator. In addition, FS-HNN models stiff, multi-timescale dynamics by decomposing the system Hamiltonian into multiple components trained on data sampled at distinct temporal resolutions. Further theoretical details are provided in Appendix A.

4.1 Structure-Preserving Hamiltonian Formulation

Hamiltonian systems can be written in symplectic form (Goldstein et al., 2002) as

$$\frac{\partial z}{\partial t} = J \frac{\delta H}{\delta z}, \quad (11)$$

where z denotes the system state and J is a skew-symmetric symplectic operator.

For ODE systems, $z = (p, q)$ (i.e., the concatenation of generalized position and momentum) is finite dimensional and the symplectic operator takes the canonical form,

$$J = \begin{bmatrix} 0 & -\mathbf{I} \\ \mathbf{I} & 0 \end{bmatrix}. \quad (12)$$

In contrast, for PDEs, z is a continuous field and J is typically a skew-symmetric differential operator (e.g., ∂_x) that depends on the equation family, boundary condition, and discretization scheme (Bridges, 1997; Bridges & Reich, 2001). As a result, there is rarely a closed-form expression for the symplectic operator for PDE systems.

To address this challenge, our method learns the action of the structure operator using a surrogate neural operator \mathcal{J}_θ

$$\Delta z = \mathcal{J}_\theta (\nabla H(z)), \quad (13)$$

to avoid explicit matrix representations. We parameterize \mathcal{J}_θ using a residual convolutional neural network (He et al., 2016), as local convolutional kernels naturally capture neighborhood coupling on discretized spatial grids and can emulate differential operators.

Rather than enforcing exact symplecticity, we impose a pseudo skew-symmetry through the orthogonality constraint

$$\langle \nabla H(z), \Delta z \rangle = 0 \quad (14)$$

which we enforce by projecting the output $\widetilde{\Delta z}$ onto the subspace orthogonal to $\nabla H(z)$,

$$\Delta z = \widetilde{\Delta z} - \frac{\langle \nabla H(z), \widetilde{\Delta z} \rangle}{\langle \nabla H(z), \nabla H(z) \rangle + \xi} \nabla H(z), \quad (15)$$

where $\xi > 0$ ensures numerical stability. In the continuous-time limit, this constraint implies conservation of the Hamiltonian

$$\frac{d}{dt} H(z) = \langle \nabla H(z), \dot{z} \rangle = 0. \quad (16)$$

The Hamiltonian H is approximated using DeepONet (Lu et al., 2021) enabling flexible representation of nonlinear functionals under varying discretizations and boundary conditions. Gradients are computed using automatic differentiation (Paszke et al., 2017). Together, the learned Hamiltonian and skew-symmetric operator define a structure-preserving HNN framework applicable to both ODE and PDE systems.

4.2 Frequency-Separated Hamiltonian Parameterization

We consider Hamiltonian systems exhibiting slow-fast dynamics by decomposing the configuration variables as $q = (q^s, q^f)$, where q^s denotes slow coordinates and q^f fast (stiff) coordinates. Accordingly, the potential term can be written as the sum of a coupled component and a stiff fast component,

$$U(q) = V(q^s, q^f) + \frac{1}{\varepsilon} \bar{W}(q^f), \quad 0 < \varepsilon \ll 1, \quad (17)$$

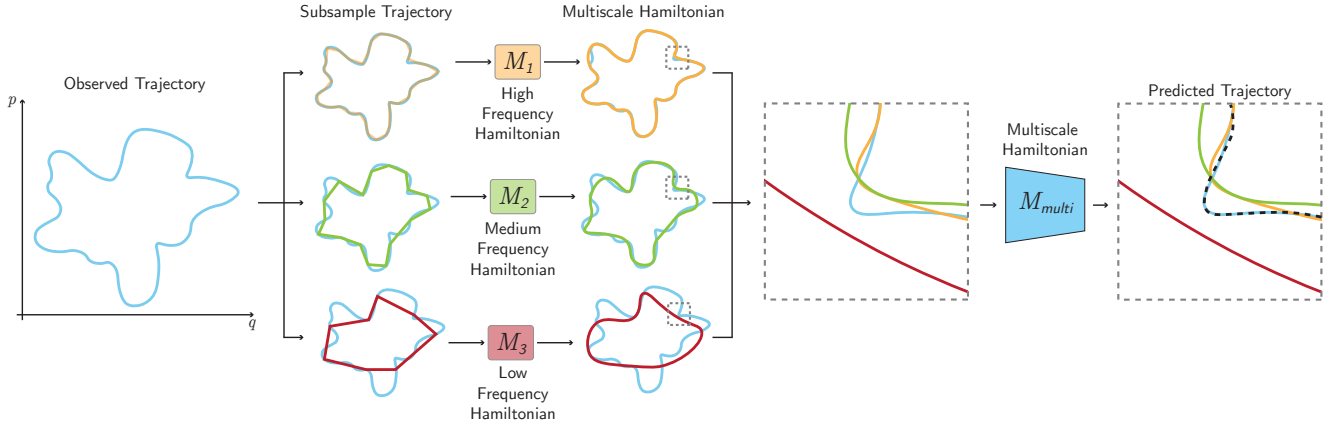


Figure 1: **Frequency-Separable Hamiltonian Neural Network.** Hamiltonian systems that exhibit dynamics with multiple timescales and be decoupled into subsystems each representing one timescale. An observation u_{train} is subsampled using interval I_1 , I_2 , and I_3 to form subsampled dataset $u^{(k)}$. The single scale HNN \mathcal{M}_k is trained on subsampled data individually. The multiscale model $\mathcal{M}_{\text{multi}}$ combines pretrained single scale HNN trajectories to predict rollout on the original resolution.

where the factor $1/\varepsilon$ encodes the relative speed of fast components. Assuming a quadratic kinetic energy with block-diagonal mass matrix $M = \text{diag}(M_s, M_f)$ and conjugate momenta $p^s = M_s \dot{q}^s$, $p^f = M_f \dot{q}^f$, the Hamiltonian takes the form

$$H(q^s, q^f, p^s, p^f) = \frac{1}{2}(p^s)^\top M_s^{-1} p^s + \frac{1}{2}(p^f)^\top M_f^{-1} p^f + V(q^s, q^f) + \frac{1}{\varepsilon} \bar{W}(q^f), \quad (18)$$

where the kinetic energy separates into slow and fast components and $\varepsilon^{-1} \bar{W}(q^f)$ captures the stiff fast potential. Hamilton's equations therefore gives the slow-fast dynamics

$$\begin{aligned} \dot{q}^s &= M_s^{-1} p^s, \\ \dot{p}^s &= -\partial_{q^s} V(q^s, q^f), \\ \dot{q}^f &= M_f^{-1} p^f, \\ \dot{p}^f &= -\partial_{q^f} V(q^s, q^f) - \varepsilon^{-1} \nabla \bar{W}(q^f) \end{aligned} \quad (19)$$

where the fast subsystem is driven by an $\mathcal{O}(\varepsilon^{-1})$ stiff force. Linearizing near a local minimizer q_*^f of \bar{W} yields the leading fast oscillator

$$\ddot{\eta} \approx -\varepsilon^{-1} M_f^{-1} K_f \eta, \quad K_f = \nabla^2 \bar{W}(q_*^f), \quad (20)$$

implying characteristic fast frequencies $\omega \sim \varepsilon^{-1/2}$. When $V = V(q^s)$, the Hamiltonian separates and the slow and fast subsystems decouple.

Leveraging this observation, we parameterize the overall system Hamiltonian as the sum of K single scale components,

$$H = \sum_{k=1}^K \mathcal{M}_k(z^{(k)}), \quad (21)$$

where each single scale Hamiltonian model \mathcal{M}_k captures the effective dynamics dominant at a particular timescale with subsampling interval I_k . $z^{(k)} = [q^{(k)}, p^{(k)}]$ represents the generalized position and momentum of the system with subsampling interval I_k . In practice, temporal subsampling acts as an implicit frequency filter - data sampled at

coarser resolutions suppress high-frequency oscillations while preserving slower modes. We exploit this property by training each component Hamiltonian \mathcal{M}_k on data sampled at a distinct temporal resolution. In practice, however, we observe that the overall system Hamiltonian is not a simple summation of single scale systems. As such we learn a mapping between the single scale Hamiltonians to the overall system Hamiltonian such that

$$H(z) = \mathcal{M}_{\text{multi}}(\mathcal{M}_1(z), \dots, \mathcal{M}_K(z)), \quad (22)$$

where $\mathcal{M}_{\text{multi}}$ is parameterized as an MLP. Hence, the resulting dynamics are governed by

$$\dot{z} = J\nabla_z \mathcal{M}_{\text{multi}}. \quad (23)$$

Figure 1 illustrates the forward pass of the proposed architecture with three distinct subsampling intervals. Given a training dataset u_{train} , time step Δt , and subsampling intervals I_1, I_2, I_3 , we form three subsampled datasets $u^{(k)}$ by taking every I_k -th snapshot of u_{train} for $k \in \{1, 2, 3\}$. Each single scale HNN \mathcal{M}_k is trained on the subsampled set $u^{(k)}$ individually. The multiscale model $\mathcal{M}_{\text{multi}}$ combines the pretrained single scale HNN to predict rollout trajectories on the full resolution data.

5 Experiments

In this section, we empirically evaluate FS-HNN on both ODE and PDE benchmarks exhibiting chaotic and/or multiscale dynamics. Across all tasks, we assess long-horizon rollout accuracy and qualitative trajectory fidelity. We compare against both black-box and structure-preserving baselines. FS-HNN results are reported for a fixed

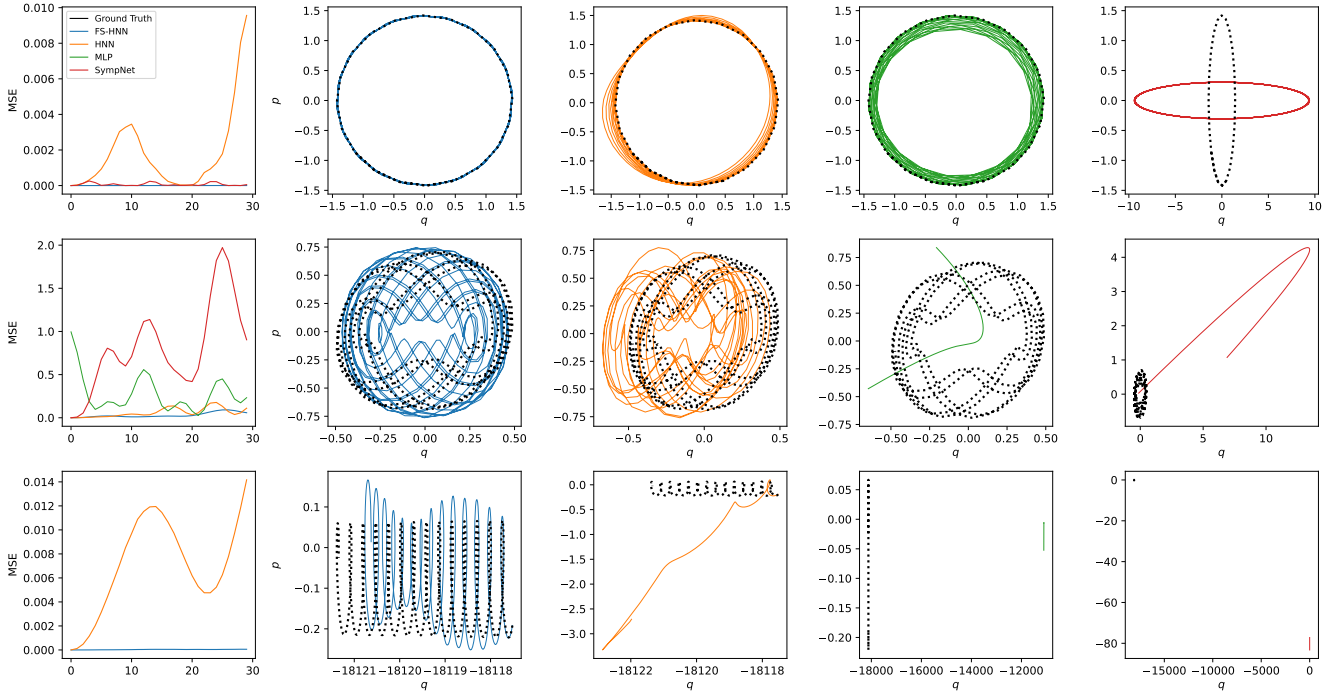


Figure 2: **Phase space comparison for ODE systems.** We show the MSE error and phase space portraits of the predicted rollout of FS-HNN, MLP, HNN (Greydanus et al., 2019), and SympNet (Jin et al., 2020) for the **(Top)** ideal pendulum, **(Middle)** double pendulum, and **(Bottom)** Fermi-Pasta-Uam-Tsingou systems. FS-HNN achieves significantly lower prediction error compared to baseline networks. Some baselines are omitted from the MSE plot due to excessively large predictive error. Exact trajectory prediction results can be checked in Figure 6 in Appendix C.

sampling scheme, the trajectory prediction accuracy under different sampling frequencies is reported in Table 3 in Appendix C.

5.1 ODE Systems

We evaluate FS-HNN on ODE systems to assess the predictive accuracy and conservation of energy. Specifically, we consider the ideal pendulum, double pendulum, and the Fermi-Pasta-Ulam-Tsingou (FPUT) system Fermi et al. (1955). We compare FS-HNN against a black-box MLP, HNN (Greydanus et al., 2019), and SympNet (Jin et al., 2020). The accuracy of the predicted trajectories is reported in Table 1 and Figure 6 and the total energy of the learned systems is reported in Figure 4 in Appendix C. Models are trained on the first 10 steps and rolled out for 1000 steps.

Pendulum. We begin with the ideal pendulum as a controlled sanity check for long-horizon rollout accuracy on a simple conservative system. Training trajectories are generated using a symplectic leapfrog integrator Iserles (1986) (see Appendix B.1 for additional details). Figure 2 compares phase-space rollouts from our method and the baselines (HNN, MLP, and SympNet). Our method produces trajectories that remain stable over long horizons and exhibits reduced energy drift relative to the baselines (see Appendix C). Quantitative rollout MSE is reported in Table 1, where our method achieves the lowest error. The parameter sizes across different models were chosen to be as comparable as possible to ensure a fair comparison, which can be checked in Table 4 of Appendix D.

Double pendulum. We next consider the double pendulum, a chaotic conservative system with increased dimensionality and strong sensitivity to initial conditions, which is known to be more challenging than the single-pendulum case Eichelsdörfer et al. (2021). Training trajectories are generated using a semi-implicit symplectic Euler integrator, and Gaussian noise is added to the initial conditions to promote robustness (see Appendix B.2 for additional details). Figure 2 and Table 1 report phase-space rollouts and quantitative errors respectively. Consistent with the pendulum results, our method achieves the lowest long-horizon rollout error and produces more stable trajectories than all baseline models.

Table 1: **Rollout accuracy for ODE systems.** We report the rollout MSE error of FS-HNN, MLP, HNN (Greydanus et al., 2019), and SympNet (Jin et al., 2020) on the pendulum, double pendulum, and Fermi-Pasta-Ulam systems. We evaluate single resolution FS-HNN (trained on only low, medium, or high resolution data) as well as the multiscale FS-HNN (trained on all frequencies). Both single resolution and multiscale FS-HNN achieves significantly lower prediction error compared to baseline networks.

Model	Res.	Pendulum	Double Pendulum	Fermi-Pasta-Ulam-Tsingou
MLP	Low	5.24×10^{-2}	6.47×10^0	1.99×10^{-1}
	Med	1.27×10^{-3}	1.28×10^0	2.39×10^{-2}
	High	1.40×10^{-4}	4.99×10^{-1}	1.98×10^{-2}
HNN	Low	2.10×10^0	1.60×10^0	2.63×10^{-2}
	Med	1.05×10^{-1}	8.67×10^{-1}	1.28×10^{-2}
	High	8.06×10^{-4}	5.93×10^{-1}	1.07×10^{-2}
	Com.	3.67×10^{-4}	3.39×10^{-1}	3.95×10^{-3}
SympNet	High	1.90×10^0	6.35×10^{-1}	2.63×10^{-3}
FS-HNN	Low	7.78×10^{-2}	1.13×10^0	5.45×10^{-2}
	Med	8.38×10^{-3}	3.45×10^{-1}	2.69×10^{-3}
	High	1.38×10^{-4}	2.71×10^{-1}	5.81×10^{-4}
	Com.	2.30×10^{-5}	2.34×10^{-2}	9.10×10^{-5}

Fermi–Pasta–Ulam–Tsingou. Finally, we evaluate our method on the Fermi–Pasta–Ulam–Tsingou (FPUT) system, a nonlinear many-body Hamiltonian benchmark known for its slow energy exchange across modes and long-term near-integrable behavior Fermi et al. (1955). The FPUT chain consists of a one-dimensional lattice of N identical masses coupled by nonlinear nearest-neighbor springs, and is widely used to assess long-horizon stability and energy transfer in multiscale Hamiltonian dynamics. Dataset generation details are provided in Appendix B.3. Figure 2 and Table 1 report rollout trajectories and quantitative errors, respectively, where our model achieves lower long-horizon prediction error than all baseline models.

We additionally evaluate energy drift for all models, with the results reported in Appendix C. To assess robustness with respect to the frequency decomposition, we varied the temporal sampling intervals used to define the component Hamiltonians. Across a range of interval choices, FS-HNN exhibits comparable predictive accuracy and stability, indicating that performance is not sensitive to a specific frequency partition (see Appendix C for additional details).

5.2 PDE Systems

We evaluate FS-HNN on PDE systems to assess generalization beyond finite-dimensional Hamiltonian systems.

Specifically, we consider the two-dimensional shallow water equations (SWE) (Vreugdenhil, 2013) under Gaussian-pulse and random initializations, as well as the incompressible Taylor–Green vortex (Taylor & Green, 1937). The 2D SWE is inviscid and unforced, and is therefore approximately conservative (up to discretization error). In contrast, the incompressible Taylor–Green vortex is viscous and exhibits energy decay over time. Together these systems test both structure preserving and non-conservative dynamics. We compare against Pseudo Hamiltonian Neural Network (PHNN) (Eidnes & Lye, 2024) and Fourier Neural Operator (FNO) (Li et al., 2020). The accuracy of the predicted flow fields is reported in Table 2. Models are trained on the first 5 steps and rolled out for the subsequent 50 steps.

2D SWE with Gaussian-pulse initial condition. We use the 2D SWE with a Gaussian-pulse initial condition to evaluate the predictive performance of FS-HNN on an inviscid, unforced system that is (approximately) conservative (Tadmor & Zhong, 2008). We simulate the 2D SWE on a periodic square domain using a second-order Heun (RK2) scheme. Additional details on the training data are provided in Appendix B.5. Figure 3 compares the learned flow fields from FS-HNN and the baselines. FS-HNN generates fields that are qualitatively consistent with the ground truth. Quantitative predictive errors are reported in Table 2, where FS-HNN achieves lower error than both PHNN and FNO.

2D SWE with random initial condition. We use the 2D SWE with random free-surface perturbations as initial conditions to evaluate the predictive performance of FS-HNN on an inviscid, unforced system that is (approximately)

Table 2: **Rollout accuracy for PDE systems.** We report the rollout MSE error of FS-HNN, PHNN (Eidnes & Lye, 2024), and FNO (Li et al., 2020) on the SWE under pulse initial condition, SWE under random initial condition, and Taylor-Green vortex. We evaluate single resolution FS-HNN (trained on only low, medium, or high resolution data) as well as the multiscale FS-HNN (trained on all frequencies). Both single resolution and multiscale FS-HNN achieves significantly lower prediction error compared to baseline networks.

Model	Res.	SWE Pulse	SWE Random	Taylor-Green
PHNN	High	8.57×10^2	1.10×10^0	3.43×10^{-4}
FNO	High	5.31×10^{-3}	2.75×10^{-2}	3.43×10^{-4}
FS-HNN	Low	1.31×10^{-2}	2.73×10^{-2}	4.95×10^{-7}
	Med	3.75×10^{-3}	8.31×10^{-4}	1.91×10^{-7}
	High	5.71×10^{-4}	1.36×10^{-4}	8.33×10^{-8}
	Com.	3.67×10^{-4}	1.40×10^{-5}	5.01×10^{-8}

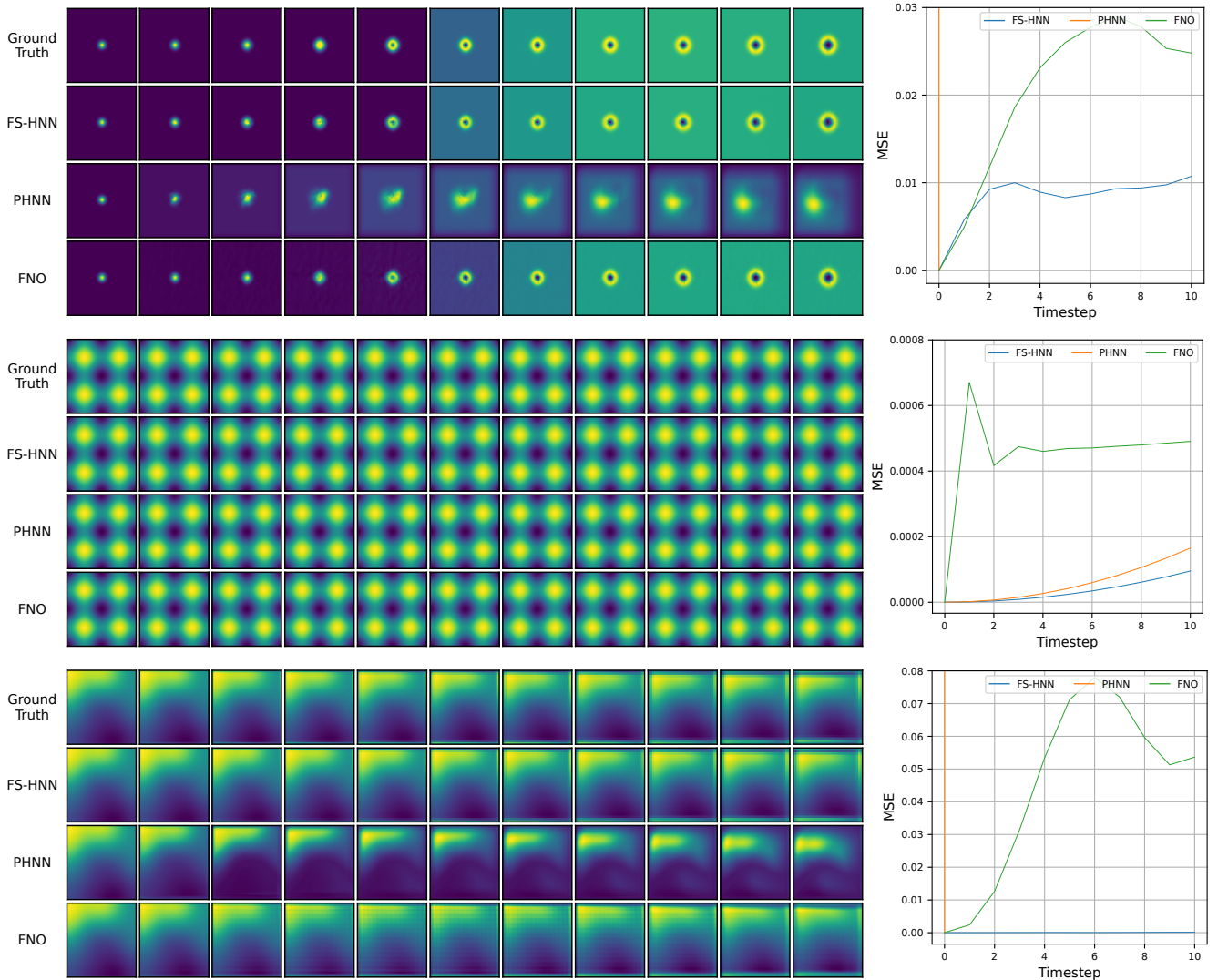


Figure 3: **Flow field comparison for PDE systems.** We report the rollout MSE error of FS-HNN, PHNN (Eidnes & Lye, 2024), and FNO (Li et al., 2020) on the **(Top)** SWE with Gaussian pulse initialization, **(Middle)** Taylor-Green vortex systems, and **(Bottom)** SWE with random initialization. FS-HNN learns qualitatively similar flow fields and achieves significantly lower prediction error compared to baseline networks. Results are plotted for the potential height(SWE)/pressure distribution(Taylor-Green) channel, results for the remaining states are given in Figure 7 in Appendix D.

conservative. Compared to the Gaussian-pulse initialization, randomly initialized systems are typically more difficult to learn (Brecht et al., 2025). We simulate the 2D SWE on a periodic square domain using a second-order Heun (RK2) scheme. Additional details on the training data are provided in Appendix B.4. Figure 3 compares the learned flow fields from FS-HNN and the baselines; FS-HNN generates fields that are qualitatively consistent with the ground truth. Quantitative predictive errors are reported in Table 2, where FS-HNN achieves lower error than both PHNN and FNO.

Incompressible Taylor–Green vortex. We use the incompressible Taylor–Green vortex to evaluate the predictive performance of FS-HNN on a viscous system that exhibits energy decay over time. We simulate the Taylor–Green vortex on a periodic square domain using a fourth-order Runge–Kutta (RK4) scheme. Additional details on the training data are provided in Appendix B.6. Figure 3 compares the learned flow fields from FS-HNN and the baselines; FS-HNN generates fields that are qualitatively consistent with the ground truth. Quantitative predictive errors are reported in Table 2, where FS-HNN achieves lower error than both PHNN and FNO.

We also evaluated the energy drift of all models; the results are reported in Appendix D. Moreover, the frequency partition is not fixed: we tested FS-HNN using different time intervals, and different combinations yielded comparable results. Additional details can be found in Appendix D.

6 Conclusion and Discussion

In this paper, we propose FS-HNN, a frequency-separable Hamiltonian neural network for nonlinear, multi-timescale dynamics. FS-HNN learns multiple Hamiltonian components from trajectories subsampled at different temporal resolutions, and combines them to reconstruct full-resolution dynamics. To improve expressiveness in complex regimes, we approximate the Hamiltonian functional using DeepONet. We further extend Hamiltonian learning to discretized PDE settings by learning the action of a skew-symmetric operator, enabling structure-preserving training for two-dimensional flow fields. Across a range of ODE and PDE benchmarks, FS-HNN improves long-horizon rollout accuracy and more faithfully captures physically meaningful behavior compared to existing baseline methods. Experimental results suggest that frequency-separated structure-preserving models provide a promising direction for learning complex multiscale physical dynamics.

Limitations and future directions Our current limitations primarily relate to dataset fidelity and computational cost. In the PDE experiments, the numerical solvers used for data generation are only approximately conservative, which may introduce discretization-induced deviations from ideal structure-preserving dynamics. While our learned skew-symmetric operator helps mitigate these effects, it remains an open question whether training on strictly conservative datasets would further improve predictive performance. In addition, enforcing the orthogonality constraint requires additional projection operations during training, which increase computational overhead. Future work will explore efficient parameterizations of the operator structure that retain physical interpretability while reducing runtime cost.

References

- Christine Allen-Blanchette. Hamiltonian gan. In *6th Annual Learning for Dynamics & Control Conference*, pp. 1662–1674. PMLR, 2024.
- Christine Allen-Blanchette, Sushant Veer, Anirudha Majumdar, and Naomi Ehrich Leonard. Lagnetvip: A lagrangian neural network for video prediction. *arXiv preprint arXiv:2010.12932*, 2020.
- Atilim Gunes Baydin, Barak A Pearlmutter, Alexey Andreyevich Radul, and Jeffrey Mark Siskind. Automatic differentiation in machine learning: a survey. *Journal of machine learning research*, 18(153):1–43, 2018.
- Tom Bertalan, Felix Dietrich, Igor Mezić, and Ioannis G Kevrekidis. On learning hamiltonian systems from data. *Chaos: An Interdisciplinary Journal of Nonlinear Science*, 29(12), 2019.
- Jiri Blazek. *Computational fluid dynamics: principles and applications*. Butterworth-Heinemann, 2015.
- Rüdiger Brecht, Elsa Cardoso-Bihlo, and Alex Bihlo. Physics-informed neural networks for tsunami inundation modeling. *Journal of Computational Physics*, 536:114066, 2025.
- Thomas J Bridges. Multi-symplectic structures and wave propagation. In *Mathematical Proceedings of the Cambridge Philosophical Society*, volume 121, pp. 147–190. Cambridge University Press, 1997.

- Thomas J Bridges and Sebastian Reich. Multi-symplectic integrators: numerical schemes for hamiltonian pdes that conserve symplecticity. *Physics Letters A*, 284(4-5):184–193, 2001.
- Steven L Brunton, Joshua L Proctor, and J Nathan Kutz. Discovering governing equations from data by sparse identification of nonlinear dynamical systems. *Proceedings of the national academy of sciences*, 113(15):3932–3937, 2016.
- Joshua William Burby, Qi Tang, and Romit Maulik. Fast neural poincaré maps for toroidal magnetic fields. *Plasma Physics and Controlled Fusion*, 63(2):024001, 2020.
- Alberto S Cattaneo, Benoit Dherin, and Alan Weinstein. Symplectic microgeometry ii: generating functions. *Bulletin of the Brazilian Mathematical Society, New Series*, 42(4):507–536, 2011.
- Paul J Channell and Clint Scovel. Symplectic integration of hamiltonian systems. *Nonlinearity*, 3(2):231, 1990.
- Renyi Chen and Molei Tao. Data-driven prediction of general hamiltonian dynamics via learning exactly-symplectic maps. In *International conference on machine learning*, pp. 1717–1727. PMLR, 2021.
- Ricky TQ Chen, Yulia Rubanova, Jesse Bettencourt, and David K Duvenaud. Neural ordinary differential equations. *Advances in neural information processing systems*, 31, 2018.
- Zhengdao Chen, Jianyu Zhang, Martin Arjovsky, and Léon Bottou. Symplectic recurrent neural networks. *arXiv preprint arXiv:1909.13334*, 2019.
- Miles Cranmer, Sam Greydanus, Stephan Hoyer, Peter Battaglia, David Spergel, and Shirley Ho. Lagrangian neural networks. *arXiv preprint arXiv:2003.04630*, 2020.
- Thai Duong, Abdullah Altawaitan, Jason Stanley, and Nikolay Atanasov. Port-hamiltonian neural ode networks on lie groups for robot dynamics learning and control. *IEEE Transactions on Robotics*, 2024.
- Jonas Eichelsdörfer, Sebastian Kaltenbach, and Phaedon-Stelios Koutsourelakis. Physics-enhanced neural networks in the small data regime. *arXiv preprint arXiv:2111.10329*, 2021.
- Solve Eidnes and Kjetil Olsen Lye. Pseudo-hamiltonian neural networks for learning partial differential equations. *Journal of Computational Physics*, 500:112738, 2024.
- Jonathan P Epperlein, Bassam Bamieh, and Karl J Astrom. Thermoacoustics and the rijke tube: Experiments, identification, and modeling. *IEEE Control Systems Magazine*, 35(2):57–77, 2015.
- Junaid Farooq, Danish Rafiq, Pantelis R Vlachas, and Mohammad Abid Bazaz. Refreshnet: learning multiscale dynamics through hierarchical refreshing. *Nonlinear Dynamics*, 112(16):14479–14496, 2024.
- Enrico Fermi, P Pasta, Stanislaw Ulam, and Mary Tsingou. Studies of the nonlinear problems. Technical report, Los Alamos National Laboratory (LANL), Los Alamos, NM (United States), 1955.
- Marc Finzi, Samuel Stanton, Pavel Izmailov, and Andrew Gordon Wilson. Generalizing convolutional neural networks for equivariance to lie groups on arbitrary continuous data. In *International conference on machine learning*, pp. 3165–3176. PMLR, 2020a.
- Marc Finzi, Ke Alexander Wang, and Andrew G Wilson. Simplifying hamiltonian and lagrangian neural networks via explicit constraints. *Advances in neural information processing systems*, 33:13880–13889, 2020b.
- Nicholas Galioto and Alex A Gorodetsky. Bayesian identification of hamiltonian dynamics from symplectic data. In *2020 59th IEEE Conference on Decision and Control (CDC)*, pp. 1190–1195. IEEE, 2020a.
- Nicholas Galioto and Alex Arkady Gorodetsky. Bayesian system id: optimal management of parameter, model, and measurement uncertainty. *Nonlinear Dynamics*, 102(1):241–267, 2020b.

- Herbert Goldstein, Charles P. Poole, and John L. Safko. *Classical Mechanics*. Addison-Wesley, 3 edition, 2002. ISBN 9780201657029.
- Samuel Greydanus, Misko Dzamba, and Jason Yosinski. Hamiltonian neural networks. *Advances in neural information processing systems*, 32, 2019.
- Chen-Di Han, Bryan Glaz, Mulugeta Haile, and Ying-Cheng Lai. Adaptable hamiltonian neural networks. *Physical Review Research*, 3(2):023156, 2021.
- Kaiming He, Xiangyu Zhang, Shaoqing Ren, and Jian Sun. Deep residual learning for image recognition. In *Proceedings of the IEEE conference on computer vision and pattern recognition*, pp. 770–778, 2016.
- Sepp Hochreiter and Jürgen Schmidhuber. Long short-term memory. *Neural computation*, 9(8):1735–1780, 1997.
- Philipp Horn, Veronica Saz Ulibarrena, Barry Koren, and Simon Portegies Zwart. A generalized framework of neural networks for hamiltonian systems. *Journal of Computational Physics*, 521:113536, 2025.
- Yifan Hu, Peiyuan Liu, Peng Zhu, Dawei Cheng, and Tao Dai. Adaptive multi-scale decomposition framework for time series forecasting. In *Proceedings of the AAAI Conference on Artificial Intelligence*, volume 39, pp. 17359–17367, 2025.
- Arieh Iserles. Generalized leapfrog methods. *IMA Journal of Numerical Analysis*, 6(4):381–392, 1986.
- Pengzhan Jin, Zhen Zhang, Aiqing Zhu, Yifa Tang, and George Em Karniadakis. Sympnets: Intrinsic structure-preserving symplectic networks for identifying hamiltonian systems. *Neural Networks*, 132:166–179, 2020.
- Michael I Jordan. Serial order: A parallel distributed processing approach. In *Advances in psychology*, volume 121, pp. 471–495. Elsevier, 1997.
- Hassan K Khalil and Jessy W Grizzle. *Nonlinear systems*, volume 3. Prentice hall Upper Saddle River, NJ, 2002.
- Yoonsang Lee and Bjorn Engquist. Variable step size multiscale methods for stiff and highly oscillatory dynamical systems. *arXiv preprint arXiv:1304.4336*, 2013.
- Zongyi Li, Nikola Kovachki, Kamyar Azizzadenesheli, Burigede Liu, Kaushik Bhattacharya, Andrew Stuart, and Anima Anandkumar. Fourier neural operator for parametric partial differential equations. *arXiv preprint arXiv:2010.08895*, 2020.
- Jiayin Liu, Yulong Yang, Vineet Bansal, and Christine Allen-Blanchette. Physically plausible multi-system trajectory generation and symmetry discovery. *arXiv preprint arXiv:2509.23003*, 2025.
- Lu Lu, Pengzhan Jin, Guofei Pang, Zhongqiang Zhang, and George Em Karniadakis. Learning nonlinear operators via deepnet based on the universal approximation theorem of operators. *Nature machine intelligence*, 3(3): 218–229, 2021.
- Michael Lutter, Christian Ritter, and Jan Peters. Deep lagrangian networks: Using physics as model prior for deep learning. *arXiv preprint arXiv:1907.04490*, 2019.
- Pierre Magal and Glenn Webb. The parameter identification problem for sir epidemic models: identifying unreported cases. *Journal of mathematical biology*, 77(6):1629–1648, 2018.
- Jan Mandel and Seymour V Parter. On the multigrid f-cycle. *Applied mathematics and computation*, 37(1):19–36, 1990.
- Jan Mandel, Steve McCormick, and John Ruge. An algebraic theory for multigrid methods for variational problems. *SIAM Journal on Numerical Analysis*, 25(1):91–110, 1988.
- Jerry B Marion. *Classical dynamics of particles and systems*. Academic Press, 2013.

- Justice Mason, Christine Allen-Blanchette, Nicholas Zolman, Elizabeth Davison, and Naomi Leonard. Learning interpretable dynamics from images of a freely rotating 3d rigid body. *arXiv preprint arXiv:2209.11355*, 2022.
- Justice J Mason, Christine Allen-Blanchette, Nicholas Zolman, Elizabeth Davison, and Naomi Ehrich Leonard. Learning to predict 3d rotational dynamics from images of a rigid body with unknown mass distribution. *Aerospace*, 10(11):921, 2023.
- Thomas Müller, Alex Evans, Christoph Schied, and Alexander Keller. Instant neural graphics primitives with a multiresolution hash encoding. *ACM transactions on graphics (TOG)*, 41(4):1–15, 2022.
- Sina Ober-Blöbaum, Theresa Wenger, Tobias Gail, and Sigrid Leyendecker. Variational multirate integrators. *arXiv preprint arXiv:2406.12991*, 2024.
- Juan A Paredes, Yulong Yang, and Dennis S Bernstein. Output-only identification of self-excited systems using discrete-time lur’e models with application to a gas-turbine combustor. *International Journal of Control*, 97(2):187–212, 2024.
- Adam Paszke, Sam Gross, Soumith Chintala, Gregory Chanan, Edward Yang, Zachary DeVito, Zeming Lin, Alban Desmaison, Luca Antiga, and Adam Lerer. Automatic differentiation in pytorch. 2017.
- Nasim Rahaman, Aristide Baratin, Devansh Arpit, Felix Draxler, Min Lin, Fred Hamprecht, Yoshua Bengio, and Aaron Courville. On the spectral bias of neural networks. In *International conference on machine learning*, pp. 5301–5310. PMLR, 2019.
- Maziar Raissi, Paris Perdikaris, and George E Karniadakis. Physics-informed neural networks: A deep learning framework for solving forward and inverse problems involving nonlinear partial differential equations. *Journal of Computational physics*, 378:686–707, 2019.
- Riley J Richards, Yulong Yang, Juan A Paredes, and Dennis S Bernstein. Output-only identification of lur’e systems with hysteretic feedback nonlinearities. In *2024 American Control Conference (ACC)*, pp. 2891–2896. IEEE, 2024.
- Eitan Tadmor and Weigang Zhong. Energy-preserving and stable approximations for the two-dimensional shallow water equations. In *Mathematics and Computation, a Contemporary View: The Abel Symposium 2006 Proceedings of the Third Abel Symposium, Alesund, Norway, May 25–27, 2006*, pp. 67–94. Springer, 2008.
- Geoffrey Ingram Taylor and Albert Edward Green. Mechanism of the production of small eddies from large ones. *Proceedings of the Royal Society of London. Series A-Mathematical and Physical Sciences*, 158(895):499–521, 1937.
- Peter Toth, Danilo Jimenez Rezende, Andrew Jaegle, Sébastien Racanière, Aleksandar Botev, and Irina Higgins. Hamiltonian generative networks. *arXiv preprint arXiv:1909.13789*, 2019.
- Michel Verhaegen and Vincent Verdult. *Filtering and system identification: a least squares approach*. Cambridge university press, 2007.
- Cornelis Boudewijn Vreugdenhil. *Numerical methods for shallow-water flow*, volume 13. Springer Science & Business Media, 2013.
- Shiyu Wang, Haixu Wu, Xiaoming Shi, Tengge Hu, Huakun Luo, Lintao Ma, James Y Zhang, and Jun Zhou. Timemixer: Decomposable multiscale mixing for time series forecasting. *arXiv preprint arXiv:2405.14616*, 2024.
- Shu Wang, Yanbo Gao, Shuai Li, Chong Lv, Xun Cai, Chuankun Li, Hui Yuan, and Jinglin Zhang. Metricgrids: Arbitrary nonlinear approximation with elementary metric grids based implicit neural representation. In *Proceedings of the Computer Vision and Pattern Recognition Conference*, pp. 21381–21391, 2025.
- Haixu Wu, Jiehui Xu, Jianmin Wang, and Mingsheng Long. Autoformer: Decomposition transformers with auto-correlation for long-term series forecasting. *Advances in neural information processing systems*, 34:22419–22430, 2021.

- Zhi-Qin John Xu, Yaoyu Zhang, Tao Luo, Yanyang Xiao, and Zheng Ma. Frequency principle: Fourier analysis sheds light on deep neural networks. *arXiv preprint arXiv:1901.06523*, 2019.
- Junjie Yao, Yuxiao Yi, Liangkai Hang, Weizong Wang, Yaoyu Zhang, Tianhan Zhang, Zhi-Qin John Xu, et al. Solving multiscale dynamical systems by deep learning. *Computer Physics Communications*, pp. 109802, 2025.
- Yaofeng Desmond Zhong and Naomi Leonard. Unsupervised learning of lagrangian dynamics from images for prediction and control. *Advances in Neural Information Processing Systems*, 33:10741–10752, 2020.
- Yaofeng Desmond Zhong, Biswadip Dey, and Amit Chakraborty. Symplectic ode-net: Learning hamiltonian dynamics with control. *arXiv preprint arXiv:1909.12077*, 2019.

A Frequency Seperable Theory

A.1 Hamiltonian Neural Network Theory

Hamiltonian systems provide a structured way to model the time evolution of many conservative mechanical systems. The state at time t is represented by a vector

$$z(t) = \begin{bmatrix} q(t) \\ p(t) \end{bmatrix} \in \mathbb{R}^{2d},$$

where $q(t) \in \mathbb{R}^d$ collects the generalized coordinates (configuration variables) and $p(t) \in \mathbb{R}^d$ collects the corresponding generalized momenta. The system is governed by a scalar Hamiltonian function $H(q, p)$, which typically represents the total energy (e.g., kinetic plus potential energy) and encodes how the coordinates and momenta interact.

The dynamics are defined implicitly by *Hamilton's equations*,

$$\dot{q} = \frac{\partial H}{\partial p}, \quad \dot{p} = -\frac{\partial H}{\partial q}, \quad (24)$$

which should be read as follows: the rate of change of the configuration variables is determined by how the energy changes with respect to momentum, while the rate of change of momentum is driven (up to a sign) by how the energy changes with respect to configuration. This coupling between (q, p) is what produces the characteristic conservative flow of Hamiltonian dynamics in phase space.

It is often convenient to express these coupled first-order equations using a single matrix-vector form. Define the *canonical symplectic matrix*

$$J = \begin{bmatrix} 0 & \mathbf{I} \\ -\mathbf{I} & 0 \end{bmatrix}, \quad J^\top = -J, \quad (25)$$

where I denotes the $d \times d$ identity matrix. The matrix J is constant and skew-symmetric, and it encodes the canonical geometry of phase space. If we denote the gradient of the Hamiltonian with respect to the full state z by

$$\nabla_z H(z) = \begin{bmatrix} \frac{\partial H}{\partial q}(q, p) \\ \frac{\partial H}{\partial p}(q, p) \end{bmatrix},$$

then Hamilton's equations can be written compactly as the *symplectic form*

$$\dot{z} = J \nabla_z H(z). \quad (26)$$

This representation highlights that the vector field \dot{z} is obtained by applying the skew-symmetric operator J to the energy gradient. Geometrically, the flow moves along level sets of H rather than directly descending or ascending the energy landscape (in contrast to gradient flows).

A key consequence of the skew-symmetry of J is the conservation of the Hamiltonian along trajectories. Differentiating $H(z(t))$ with respect to time and applying the chain rule yields

$$\frac{dH}{dt} = \nabla_z H(z)^\top \dot{z}. \quad (27)$$

Substituting (26) into (27) gives

$$\frac{dH}{dt} = \nabla_z H(z)^\top J \nabla_z H(z). \quad (28)$$

Since $J^\top = -J$, the quadratic form $x^\top J x$ vanishes for any vector x , and therefore

$$\frac{dH}{dt} = 0. \quad (29)$$

Thus, in an ideal Hamiltonian system without external forcing or dissipation, the Hamiltonian remains constant over time, reflecting conservation of energy and the fact that the dynamics evolve on invariant energy surfaces in phase space.

The **Hamiltonian Neural Network (HNN)** framework replaces the unknown Hamiltonian H with a neural network $H_\theta(z)$. Instead of directly learning the vector field $\dot{z} = f(z)$, HNN learns the scalar Hamiltonian and recovers the dynamics through the symplectic structure:

$$\dot{z}_\theta = J\nabla_z H_\theta(z). \quad (30)$$

Given training data $\{(z_i, \dot{z}_i)\}_{i=1}^N$, the parameters θ are typically learned by minimizing

$$\mathcal{L}(\theta) = \frac{1}{N} \sum_{i=1}^N \|\dot{z}_i - J\nabla_z H_\theta(z_i)\|_2^2. \quad (31)$$

By construction, the learned vector field lies in the Hamiltonian class, which helps preserve geometric structure such as conservation properties and improves long-term stability compared with unconstrained neural ODE models.

A.2 Slow–Fast Splitting in Hamiltonian Form.

Following the multirate setting in Ober-Blöbaum et al. (2024), assume the potential energy can be additively decomposed into slow and fast parts,

$$U(q) = V(q) + W(q), \quad W(q) = \frac{1}{\varepsilon} \widetilde{W}(q), \quad 0 < \varepsilon \ll 1. \quad (32)$$

so that W generates stiff (fast) forces. Moreover, split the configuration into slow and fast variables

$$q = \begin{bmatrix} q^s \\ q^f \end{bmatrix}, \quad q^s \in Q_s, \quad q^f \in Q_f, \quad Q_s \times Q_f = Q, \quad (33)$$

and assume (i) the fast potential depends only on the fast variables, $W = W(q^f)$, while the slow potential may depend on all variables, $V = V(q^s, q^f)$, and (ii) the kinetic energy is quadratic with a block-diagonal mass matrix,

$$T(\dot{q}) = \frac{1}{2} \dot{q}^\top M \dot{q}, \quad M = \begin{bmatrix} M_s & 0 \\ 0 & M_f \end{bmatrix}. \quad (34)$$

These assumptions are exactly those used to derive the multirate formulation. Then we're gonna to split the system into two parts.

First, for the Lagrangian and conjugate momenta, with the split, the Lagrangian reads

$$L(q^s, q^f, \dot{q}^s, \dot{q}^f) = \frac{1}{2} (\dot{q}^s)^\top M_s \dot{q}^s + \frac{1}{2} (\dot{q}^f)^\top M_f \dot{q}^f - V(q^s, q^f) - W(q^f). \quad (35)$$

Define the conjugate momenta by the Legendre map

$$p^s := \frac{\partial L}{\partial \dot{q}^s} = M_s \dot{q}^s, \quad p^f := \frac{\partial L}{\partial \dot{q}^f} = M_f \dot{q}^f, \quad (36)$$

Hence,

$$\dot{q}^s = M_s^{-1} p^s, \quad \dot{q}^f = M_f^{-1} p^f. \quad (37)$$

Hence, the Hamiltonian can be obtained by the Legendre transform

$$H(q^s, q^f, p^s, p^f) = (p^s)^\top \dot{q}^s + (p^f)^\top \dot{q}^f - L(q^s, q^f, \dot{q}^s, \dot{q}^f). \quad (38)$$

with \dot{q}^s, \dot{q}^f expressed in terms of p^s, p^f using (37). Substituting (35)–(37) gives

$$H(q^s, q^f, p^s, p^f) = \frac{1}{2}(p^s)^\top M_s^{-1} p^s + \frac{1}{2}(p^f)^\top M_f^{-1} p^f + V(q^s, q^f) + W(q^f). \quad (39)$$

After this, Hamilton's equations are

$$\dot{q}^s = \frac{\partial H}{\partial p^s}, \quad \dot{p}^s = -\frac{\partial H}{\partial q^s}, \quad \dot{q}^f = \frac{\partial H}{\partial p^f}, \quad \dot{p}^f = -\frac{\partial H}{\partial q^f}. \quad (40)$$

Applying (39) yields the split system

$$\dot{q}^s = M_s^{-1} p^s, \quad \dot{p}^s = -\frac{\partial V}{\partial q^s}(q^s, q^f), \quad (41)$$

$$\dot{q}^f = M_f^{-1} p^f, \quad \dot{p}^f = -\frac{\partial V}{\partial q^f}(q^s, q^f) - \nabla W(q^f), \quad (42)$$

Now substitute the stiffness scaling (32) with $W(q^f) = \varepsilon^{-1} \bar{W}(q^f)$. Then

$$\nabla W(q^f) = \frac{1}{\varepsilon} \nabla \bar{W}(q^f), \quad (43)$$

so the fast momentum equation becomes

$$\dot{p}^f = -\frac{\partial V}{\partial q^f}(q^s, q^f) - \frac{1}{\varepsilon} \nabla \bar{W}(q^f), \quad (44)$$

making explicit that the fast subsystem is driven by an $\mathcal{O}(\varepsilon^{-1})$ force, while the slow subsystem (41) contains no such stiff term. This is the Hamiltonian mechanism behind the slow–fast separation.

At last, let q_*^f be a local minimizer of \bar{W} so that $\nabla \bar{W}(q_*^f) = 0$ and define $\eta := q^f - q_*^f$. Linearizing $\nabla \bar{W}(q^f)$ near q_*^f gives $\nabla \bar{W}(q^f) \approx K_f \eta$ with $K_f = \nabla^2 \bar{W}(q_*^f) \succeq 0$. Ignoring lower-order coupling terms in $\partial V / \partial q^f$ relative to ε^{-1} , we combine

$$\dot{q}^f = M_f^{-1} p^f, \quad \dot{p}^f \approx -\frac{1}{\varepsilon} K_f \eta$$

to obtain the leading fast oscillator

$$\ddot{\eta} \approx -\frac{1}{\varepsilon} M_f^{-1} K_f \eta. \quad (45)$$

Hence the characteristic fast frequencies scale like $\omega \sim \varepsilon^{-1/2}$, confirming that q^f evolves on a much smaller time scale than q^s .

Then the full phase-space vector would be

$$z := \begin{bmatrix} q^s \\ q^f \\ p^s \\ p^f \end{bmatrix}.$$

Then (40) can be written in canonical symplectic form

$$\dot{z} = J \nabla_z H(z), \quad J = \begin{bmatrix} 0 & 0 & \mathbf{I} & 0 \\ 0 & 0 & 0 & \mathbf{I} \\ -\mathbf{I} & 0 & 0 & 0 \\ 0 & -\mathbf{I} & 0 & 0 \end{bmatrix}, \quad (46)$$

where the block sizes match (q^s, q^f, p^s, p^f) .

Finally, if in addition the slow potential depends only on the slow variables, $V = V(q^s)$, and the kinetic energy contains no coupling between \dot{q}^s and \dot{q}^f (already ensured by (34)), then the Hamiltonian separates as

$$H(z) = H_s(q^s, p^s) + H_f(q^f, p^f),$$

and the slow and fast Hamiltonian subsystems evolve independently (and can be simulated in parallel) without exchanging information.

B Data Generation

B.1 Pendulum.

For the simple pendulum, the state is (θ, ω) with dynamics $\dot{\theta} = \omega$ and $\dot{\omega} = -(g/L) \sin \theta$. We generate data using a symplectic (leapfrog) scheme: first update ω to a half step, then advance θ , and finally update ω to the full step $(\omega_{n+\frac{1}{2}}, \theta_{n+1}, \omega_{n+1})$. A single random initial condition is sampled with $\theta_0 \sim \mathcal{U}[-\pi, \pi]$ and $\omega_0 \sim \mathcal{U}[-1, 1]$, and the system is integrated for $N_{\text{traj}} \times N_{\text{steps}}$ steps, after which the long trajectory is reshaped into N_{traj} segments. Optionally, i.i.d. Gaussian noise with standard deviation σ can be added to both q and v . The underlying continuous-time pendulum is conservative (no damping/forcing), and the leapfrog integrator is symplectic, which yields a bounded energy error and avoids systematic energy drift over long horizons.

B.2 Double Pendulum.

For the double pendulum, we represent the state as $(\theta_1, \omega_1, \theta_2, \omega_2)$ with parameters (m_1, m_2, L_1, L_2, g) . The accelerations (α_1, α_2) are computed from the standard coupled equations, and time stepping is performed by a semi-implicit *symplectic Euler* update: first update angular velocities, then update angles using the new velocities. Angles are wrapped back to $(-\pi, \pi]$ after each update to avoid unbounded growth. As in the pendulum case, we sample one random initial condition $\theta_{1,0}, \theta_{2,0} \sim \mathcal{U}[-\pi, \pi]$, $\omega_{1,0}, \omega_{2,0} \sim \mathcal{U}[-1, 1]$, evolve the system for $N_{\text{traj}} \times N_{\text{steps}}$ steps, and reshape the long roll-out into N_{traj} trajectory segments. Optional additive Gaussian noise is supported for both q and v . The continuous double pendulum (without dissipation) is energy-conserving, and the symplectic Euler discretization preserves the symplectic structure, typically producing stable long-term behavior with bounded (though not exactly zero) energy error.

B.3 Fermi-Pasta-Ulam-Tsingou.

For this 1D particle chain, the state is $(q, p) \in \mathbb{R}^N \times \mathbb{R}^N$, where q_i and p_i denote the displacement and momentum of the i -th particle (mass m). The dynamics are Hamiltonian:

$$\dot{q}_i = \frac{p_i}{m}, \quad \dot{p}_i = f_{i-1}(q) - f_i(q),$$

with periodic boundary conditions $q_{N+1} \equiv q_1$ and $q_0 \equiv q_N$ unless otherwise specified. Let $r_i(q) = q_{i+1} - q_i$ be the nearest-neighbor stretch. The (unsigned) spring force magnitude associated with bond i is

$$f_i(q) = k r_i + \alpha r_i^2 + \beta r_i^3.$$

Equivalently, the system corresponds to the Hamiltonian

$$H(q, p) = \sum_{i=1}^N \frac{p_i^2}{2m} + \sum_{i=1}^N \left(\frac{k}{2} r_i^2 + \frac{\alpha}{3} r_i^3 + \frac{\beta}{4} r_i^4 \right).$$

In many experiments we set $\alpha = 0$ and $\beta > 0$.

Data are generated using a symplectic velocity–Verlet integrator. Given (q_n, p_n) , compute the force $F(q_n)$, update positions

$$q_{n+1} = q_n + \frac{p_n}{m} \Delta t + \frac{1}{2} \frac{F(q_n)}{m} \Delta t^2,$$

recompute $F(q_{n+1})$, and then update momenta

$$p_{n+1} = p_n + \frac{1}{2}(F(q_n) + F(q_{n+1}))\Delta t.$$

A random initial condition is sampled as

$$q_0 \sim \mathcal{N}(0, \sigma_q^2 I), \quad p_0 \sim \mathcal{N}(0, \sigma_p^2 I).$$

The system is integrated for $N_{\text{traj}} \times N_{\text{steps}}$ steps with fixed Δt , saving every s steps. The resulting long roll-out is reshaped into N_{traj} trajectory segments of length

$$T = \left\lfloor \frac{N_{\text{steps}}}{s} \right\rfloor + 1.$$

Optionally, i.i.d. Gaussian noise with standard deviation σ can be added to both q and p . We also record the total energy $E = H(q, p)$ at each saved frame. The underlying continuous-time system is conservative (no damping or forcing), and the velocity–Verlet scheme is symplectic, which typically yields stable long-horizon simulations with bounded energy error rather than systematic energy drift.

B.4 2D Shallow Water Equations (SWE) with Random Initial Condition.

We generate a two-dimensional shallow-water dataset on a periodic square domain with physical parameters $L_x = L_y = 10^6$, gravity $g = 9.81$, and mean depth $H = 100$. The computational grid is uniform with $N_x = N_y = 64$, and periodicity is enforced via circular shifts in the spatial discretization. All optional source terms are disabled (Coriolis, β -effect, friction, wind, sources/sinks), yielding an inviscid, unforced configuration.

The solver evolves conservative variables (h, m_x, m_y) in flux-divergence form, where the mass equation is

$$\partial_t h = -(\partial_x m_x + \partial_y m_y),$$

and the momentum fluxes include the hydrostatic pressure contribution $\frac{1}{2}gh^2$. Time integration uses a CFL-based step size

$$dt = 0.1 \frac{\min(dx, dy)}{\sqrt{gH}},$$

together with a second-order Heun (RK2) scheme. At each saved step, diagnostic velocities are recovered as $u = m_x/h$ and $v = m_y/h$ (using a small depth floor), and the free-surface anomaly is computed as $\eta = h - H$.

Initial conditions are random free-surface perturbations η_0 constructed by averaging two Gaussian random fields and then repeatedly applying Gaussian smoothing until the maximum nearest-neighbor jump falls below a prescribed threshold, enforcing spatial regularity. We generate 1000 independent rollouts and save the resulting time series (including u , v , and the stored height field). In the continuous setting, the inviscid, unforced shallow-water equations conserve mass and admit an energy invariant; in our implementation, the conservative flux form promotes mass conservation (up to numerical error), while energy is not exactly preserved due to the explicit RK2 time stepping.

B.5 Gaussian Pulse Initial Condition under SWE

We generate a two-dimensional shallow-water dataset on a periodic square domain using the same solver and physical configuration described above (uniform 64×64 grid on $[-5 \times 10^5, 5 \times 10^5]^2$, periodic boundaries enforced via circular shifts in the spatial discretization, inviscid and unforced). The prognostic fields are the layer depth (free-surface height) $h(x, y, t)$ and the horizontal velocity components $u(x, y, t)$, $v(x, y, t)$ (equivalently the conservative variables (h, m_x, m_y) with $m_x = hu$ and $m_y = hv$). We record time series of (u, v, h) together with the corresponding time stamps t .

Unlike random-field initialization, each rollout here is initialized by a deterministic *localized Gaussian pulse* in the free-surface anomaly η_0 . On the discrete grid, we set

$$\eta_0(i, j) = A \exp\left(-\frac{(i - i_c)^2 + (j - j_c)^2}{2\sigma^2}\right),$$

with amplitude $A = 0.1$, width $\sigma = 2$ grid cells, and center (i_c, j_c) at the domain midpoint by default. The pulse is converted to the initial height field using the same convention as the implementation (e.g., $h(\cdot, \cdot, 0) = H + \eta_0$ for mean depth H), after which the shallow-water equations are integrated forward in time.

We generate 500 independent rollouts (each starting from the same centered pulse unless the center is randomized) and save the resulting arrays:

$$u \in \mathbb{R}^{N_{\text{traj}} \times N_t \times N_y \times N_x}, \quad v \in \mathbb{R}^{N_{\text{traj}} \times N_t \times N_y \times N_x}, \quad h \in \mathbb{R}^{N_{\text{traj}} \times N_t \times N_y \times N_x}, \quad t \in \mathbb{R}^{N_{\text{traj}} \times N_t},$$

together with auxiliary stored diagnostics (e.g., hm) and the constructed pulse η_0 .

In the continuous setting, the inviscid, unforced shallow-water equations conserve total mass and admit an energy invariant; in our discrete implementation, the flux-form evolution promotes near-conservation of mass up to numerical error, while exact energy conservation is not enforced due to explicit time stepping.

B.6 2D Incompressible Taylor-Green Vortex (Vorticity Formulation).

We generate an incompressible flow dataset from the 2D Taylor–Green vortex on a periodic domain of size $L = 2\pi$, discretized on a uniform $N \times N$ grid (default $N = 128$). The kinematic viscosity is set from the Reynolds number via $\nu = U_0 L / \text{Re}$. We initialize the velocity field with the classical Taylor–Green pattern

$$u(x, y, 0) = U_0 \sin(kx) \cos(ky), \tag{47}$$

$$v(x, y, 0) = -U_0 \cos(kx) \sin(ky), \tag{48}$$

with $k = 1$, and compute the initial vorticity $\omega = \partial_x v - \partial_y u$ using periodic centered differences.

The evolution is carried out in vorticity form. The streamfunction ψ is obtained spectrally by solving

$$\Delta\psi = -\omega$$

in Fourier space, and velocities are recovered as

$$(u, v) = (\partial_y \psi, -\partial_x \psi).$$

The vorticity dynamics are advanced according to

$$\partial_t \omega = -(u \partial_x \omega + v \partial_y \omega) + \nu \Delta \omega,$$

where advection is discretized with periodic centered differences and diffusion with a standard Laplacian stencil. Time integration uses a classical RK4 method, and snapshots are stored every `save_every` steps. The dataset is saved as a full time series (u, v, p) (with analytic pressure for the Taylor–Green vortex).

Unlike inviscid Hamiltonian benchmarks, this system includes viscosity ($\nu > 0$) and is therefore *not* energy-conserving: kinetic energy and enstrophy decay over time due to the diffusive term $\nu \Delta \omega$.

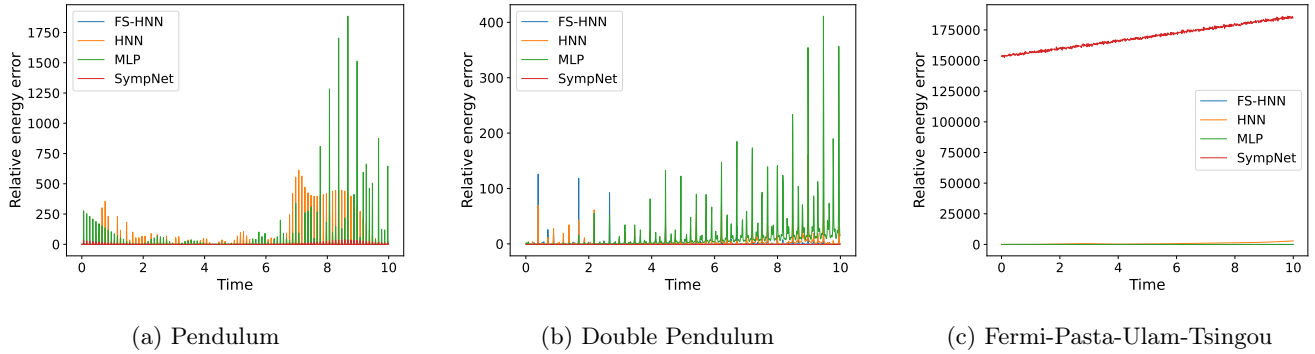


Figure 4: Relative energy deviation in ODE settings. The energy is not strictly conserved; instead, it shows a small periodic perturbation. Even so, FS-HNN matches the ground truth most closely.

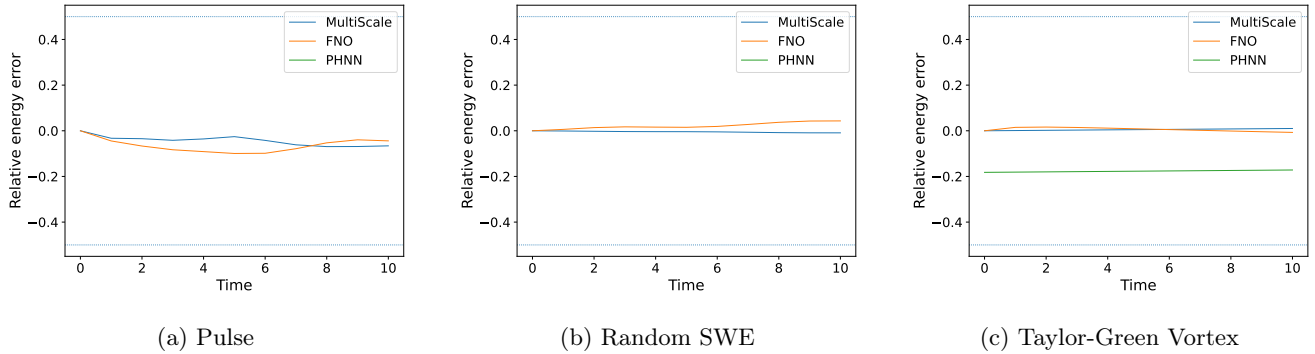


Figure 5: Relative energy deviation in PDE settings. Due to the dataset setup, energy is not strictly conserved; however, the variation remains small. We therefore report energy changes in relative terms. Overall, FS-HNN matches the ground truth most closely.

C ODE Experimental Result Supplements

Here we show the exact trajectory prediction of all benchmarks in Figure 6. The fitting performance is not perfect for every benchmark but it’s already satisfying compared with existing models.

The energy deviation from ground truth of different models is shown in Figure 4. Due to the dataset setup, energy is not strictly conserved; instead, it exhibits a small periodic perturbation. Nevertheless, FS-HNN matches the ground truth most closely.

Moreover, rollout errors for single models trained using different time intervals are reported in Table 3. In FS-HNN, each component model can be replaced with one trained at a different time interval; multiple choices yield comparable performance. The configuration used in the main text is chosen for convenience ($1\Delta t$, $2\Delta t$, and $3\Delta t$, where Δt is the time interval of the highest temporal resolution).

D PDE Experimental Result Supplements

Energy deviation from ground truth for the PDE models is shown in Figure 5, and extra visualization results of the prediction field(y-momentum, potential) are shown in Figure 7

Model parameter counts are listed in Table 4, indicating that comparisons between FS-HNN and the baselines are

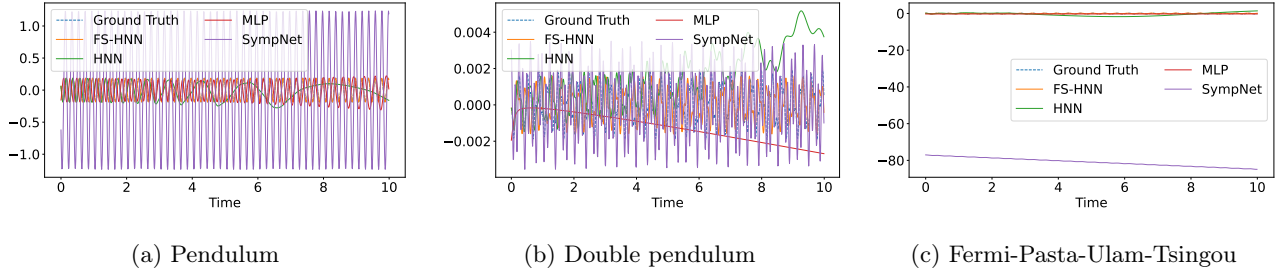


Figure 6: Exact trajectory comparisons of FS-HNN against benchmark methods. While the fit is not perfect, FS-HNN achieves satisfactory performance relative to existing models.

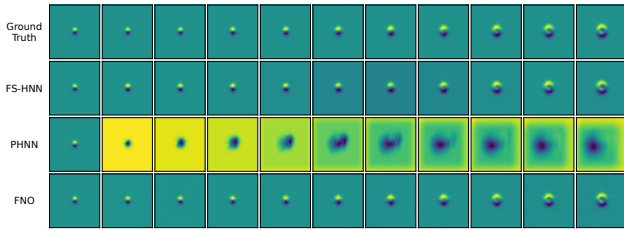
Table 3: Rollout errors across different intervals by single models of FS-HNN. Models trained at higher resolution usually achieve better fits, but this advantage diminishes as the interval becomes larger. Therefore, the choice of resolution-interval combinations does not need to be fixed.

Interval	Pendulum	Double pendulum	Fermi-Pasta	Pulse_swe	Random_swe	Taylor-Green
1dt	4.92×10^{-3}	3.44×10^{-1}	9.64×10^{-4}	5.71×10^{-4}	1.36×10^{-4}	8.33×10^{-8}
2dt	2.91×10^{-1}	4.59×10^{-1}	3.49×10^{-3}	3.75×10^{-3}	8.31×10^{-4}	1.91×10^{-7}
3dt	2.06×10^0	5.82×10^0	2.08×10^{-3}	1.31×10^{-2}	2.73×10^{-2}	4.95×10^{-7}
4dt	1.91×10^0	4.13×10^0	2.89×10^{-2}	4.12×10^{-3}	2.06×10^{-2}	2.06×10^{-5}
5dt	2.10×10^0	1.22×10^0	3.84×10^{-2}	1.32×10^{-2}	3.84×10^{-2}	4.20×10^{-5}
6dt	1.99×10^0	1.06×10^0	6.98×10^{-2}	2.72×10^{-2}	3.41×10^{-2}	3.40×10^{-5}
7dt	2.12×10^0	5.46×10^0	4.06×10^{-2}	7.56×10^{-2}	3.60×10^{-2}	4.99×10^{-5}
8dt	2.02×10^0	1.70×10^0	2.68×10^{-2}	5.35×10^{-2}	3.60×10^{-2}	2.35×10^{-5}
9dt	2.03×10^0	1.96×10^0	2.96×10^{-2}	1.54×10^0	1.08×10^{-1}	3.17×10^{-5}

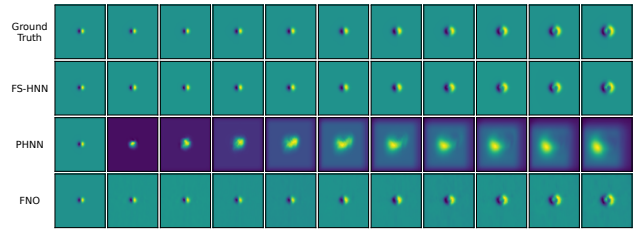
fair. Compared with traditional approaches that focus exclusively on learning the highest-resolution trajectories, we find that allocating part of the learning capacity to lower-resolution data can better capture the underlying dynamics and improve system identification.

Table 4: Model parameter count, which shows that all models are compared in a relatively fair condition. Some models are not scaled further because, as the networks become deeper and wider, their fitting performance can actually degrade. For these models, we therefore stop increasing the number of parameters

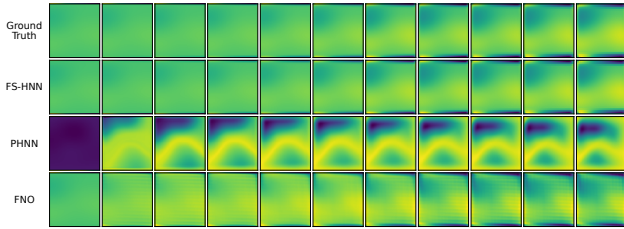
	FS-HNN(ODE)	FS-HNN(PDE)	HNN(Combined)	MLP	SympNet	PHNN	FNO
Size	3.21×10^6	2.04×10^6	2.82×10^6	1.32×10^6	0.76×10^6	4.80×10^6	4.216×10^6



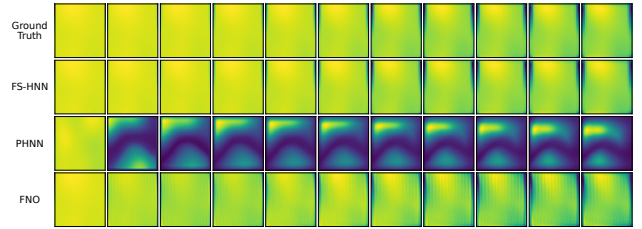
(a) X-momentum prediction of pulse



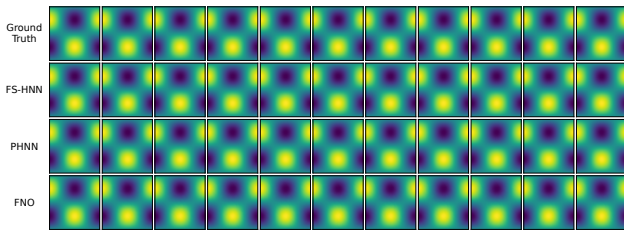
(b) Y-momentum prediction of pulse



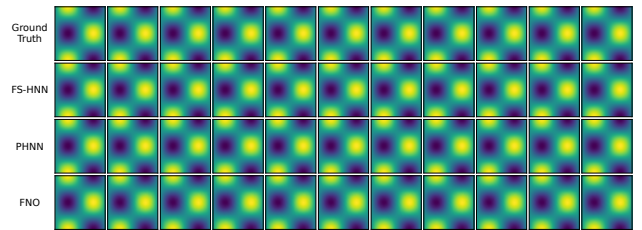
(c) X-momentum prediction of random swe



(d) Y-momentum prediction of random swe



(e) X-momentum of Taylor-Green vortex



(f) Y-momentum of Taylor-Green vortex

Figure 7: Supplementary experiment results for PDE cases. From top to bottom is ground truth, FS-HNN, PHNN and FNO.